Available online at www.sciencedirect.com
SCIENCE DIRECT®
International Journal of Multiphase Flow 31 (2005) 921–939
International Journal of Multiphase Flow
www.elsevier.com/locate/ijmulflow

Study of a free surface in open-channel water flows in the regime from "weak" to "strong" turbulence

Sergey Smolentsev *, Reza Miraghaie

Department of Mechanical and Aerospace Engineering, University of California, Los Angeles Box 951597, 43-133 Engr IV, Los Angeles, CA 90095-1597, USA

Received 1 February 2005; received in revised form 10 May 2005

Abstract

A liquid–air interface in an inclined open-channel water flows was studied experimentally as the flow changes from "weak" to "strong" turbulence. In this regime, the interface is highly agitated by bulk eddies and waves, but not broken. The surface deformation statistics were obtained under a variety of conditions, including different inclination angles and flow rates. The parameter space is described in terms of Reynolds, Froude, and Weber numbers. The surface-normal displacements were obtained via the time series of the fluctuating flow depth with an ultrasound transducer. Independently, the in-plane changes in surface structures were acquired with a high-speed camera. These structures are seen as surface cells. By applying a newly developed image processing technique, the cell celerity was found to agree well with the mean flow velocity. This suggests that the cells appear when a turbulent surface-renewal eddy interacts with the interface. As the flow changes to strong turbulence, the turbulence–interface interactions become dominant over the wave phenomena, and the turbulent structures at the surface become more 3D (similar to those in the bulk flow), compared to quasi-2D structures in the weak turbulence.

Keywords: Turbulence; Free surface; Water–air interface; Surface renewal; Image processing

* Corresponding author. Tel.: +1 310 794 5366; fax: +1 310 825 2599.
E-mail address: sergey@fusion.ucla.edu (S. Smolentsev).

0301-9322/$ - see front matter © 2005 Elsevier Ltd. All rights reserved.
doi:10.1016/j.ijmultiphaseflow.2005.05.008

1. Introduction

1.1. Background

When a liquid flows over a solid surface, the liquid–gas interface is often not flat. Wave motions, including capillary or gravity waves, can produce deformations, or deformations can be caused by turbulent eddies in the liquid impinging upon the free surface. Both mechanisms have a strong effect on the scalar transfer rate across the interface. The importance of the wave motion was demonstrated by Frisk and Davis (1972), Kutateladze (1982), and Nakoryakov et al. (1987), indicating strong correlation between the scalar transport and surface waves. An increase in the heat transfer coefficient by 40–60% due to surface waves was reported by Frisk and Davis (1972), while mass transfer intensification in absorption of carbon dioxide by 100–170% in wavy water flows was observed by Kutateladze (1982) and Nakoryakov et al. (1987). Another strong evidence of the wave effect on mass transfer was shown by Saylor and Handler (1997) in their studies of gas transport across an air–water interface populated with capillary waves. Recently, an approximately 100% increase in heat transfer coefficient due to interface irregularities was observed by Freeze et al. (2003) in inclined water flows.

Recent discoveries in studies of turbulence in open-channel flows near the liquid–gas interface have shown that if large shear stresses are not applied to the free surface, the scalar (heat and mass) transport rate across the interface is mostly controlled by large turbulent eddies coming from the interior flow. Such eddies are formed as a result of bursting events in the near-wall region. The turbulent eddies reach the interface, and then gradually dissipate, and/or attach themselves to the surface before being dissipated. This process of delivering liquid from the flow interior to the free surface by turbulent eddies is known as "surface-renewal phenomenon" (Dankwerts, 1951). The importance of this phenomenon can be illustrated by the fact that the mass transfer coefficient across the interface is proportional to the square root of the surface-renewal frequency. Many characteristics of the surface-renewal eddies and associated surface phenomena were carefully studied both experimentally and numerically. As shown by Komori et al. (1989), the frequency of the surface-renewal eddies is slightly lower than the bursting frequency, indicating that almost all the wall ejections reach the interface. It was also observed (Komori et al., 1982, 1989) that at the free surface and in its vicinity, the surface-renewal eddies are about $2h_m$, $0.5h_m$, and h_m in the streamwise, vertical, and spanwise directions, respectively, where h_m is the mean flow thickness. Rashidi (1997) measured the average size of the interfacial patches associated with the upwelling eddy motion at the interface using oxygen bubble visualization technique. He observed that the patch size is comparable with the mean flow depth. The turbulent length scale near a free surface has also been calculated using DNS (e.g. Handler et al., 1993). Similar to the earlier experimental studies (Ueda et al., 1977), the DNS study showed significant turbulence redistribution near the interface. Namely, the streamwise and spanwise length scales associated with the streamwise and spanwise velocity fluctuations grow when approaching the free surface from the flow bulk, while the length scale normal to the free surface decreases. This indicates a more pancake-like eddy structure near the free surface compared with the structure in the bulk flow where turbulence is very similar to that in a closed channel flow. It was found that the increase in the streamwise length scale is by a factor of three and it is by a factor of two for the spanwise length scale, in comparison with the bulk values. Recent DNS studies by Naga-

osa and Handler (2003) have revealed that a ring-like vortex is a good representation of the characteristic structure responsible for surface-renewal. Such a ring-like vortex evolves from a hairpin vortex, as it approaches the free surface from the interior flow.

It should be noted that in all studies of turbulent free-surface flows cited above, the effect of free-surface deformation was insignificant. There is lack of data for turbulent flows where the interface is essentially disturbed. In the experimental studies, the flow conditions resulting in no or small surface deformations were realized by establishing a so-called subcritical flow regime, in which amplifying of surface disturbances does not occur. Though small in size but finite, surface displacements in the subcritical flow were detected experimentally by Rashidi (1997) by measuring the average surface rises and falls associated with the turbulent eddies impinging upon the free surface. The scaling of surface displacements due to turbulence impinging upon the free surface was also studied. It was found that they are best scaled using a mixed scale that includes a gravity effect.

Almost all the numerical DNS studies were also performed for a non-deformable interface, applying a boundary condition that neglects the surface-normal component of the velocity fluctuation. Such a boundary condition is a very strong assumption that does not completely meet the experimental observations even in a subcritical flow regime. To our knowledge, there are only two DNS studies that take into account the deformation of the free surface by turbulence–interface interactions (Borue et al., 2001; Tsai, 1998). However, in both studies the surface displacement was assumed to be small compared with the flow depth, and as a matter of fact, no differences with the non-deformable free surface flow regimes was observed.

1.2. Objective and motivation of the present study

The present research is focused on surface phenomena in inclined open-surface turbulent water flows and continues previous theoretical and experimental studies relevant to a fusion power reactor (Smolentsev et al., 2002a,b; Freeze et al., 2003; Smolentsev et al., 2004). The study is mostly motivated by the APEX (Advanced Power Extraction) Project (Abdou et al., 1999), in which liquid layers of flowing molten salts are considered as alternative to a solid wall to absorb high heat fluxes from the reactor plasma. The turbulent layer flows down the reactor First Wall with a free surface facing the plasma and absorbing the heat flux. The effectiveness of the heat removal depends significantly on interfacial processes, such as interfacial waves and turbulent mixing at a free surface. In addition to fusion applications, knowing regular trends of the near-surface motion is of primary importance for environmental applications, since a scalar transfer can be seen in many natural processes. Examples include thermal and water pollution in rivers and oceans, and recycling of heat and mass between the atmosphere and water, just as it happens in the carbon dioxide cycle of the Earth (Komori, 1996).

Unlike the free-surface turbulence studies cited above, which are related to the so-called "weak" turbulence, the present effort is aimed at studying interface phenomena in the regime where the surface deformations are not negligibly small. The terminology "weak" and "strong" turbulence, as applied to free surface flows, implies two different flow regimes, in which the turbulent liquid–gas interface is almost not disturbed or, on the contrary, highly agitated by turbulent structures. The appearance of weak or strong turbulence depends on the stabilizing effect of capillary and gravity forces against the disrupting influence of the turbulent kinetic energy. The

key dimensionless parameters, which are responsible for the free surface regime, are therefore the turbulent Weber and Froude numbers built through the length scale L and the overall velocity q of a typical turbulent element of fluid near the free surface, such that $We_t = q^2 L\rho/2\sigma$ and $Fr_t = q/\sqrt{2gL}$. Hereinafter, ρ, σ, ν and g are the fluid density, surface tension, kinematic viscosity and acceleration due to gravity respectively. The special form of the Weber and Froude numbers matches those in the paper by Brocchini and Peregrine (2001). These authors suggest a convenient way of approximate characterization of the free surface regime, based on a so-called "L–q diagram". Such a diagram, adapted to the present experimental conditions, is shown in Fig. 1. In the diagram, q is identified with the friction velocity: $U_* = \sqrt{\tau_w/\rho}$, where τ_w is the wall stress. The mean flow thickness is used as a turbulent length scale L, assuming that the representative turbulent eddy size is comparable with the characteristic flow dimension. The (L, q)-plane is subdivided into four regions by two dotted lines, which are simply defined by critical values of We_t and Fr_t obtained from the energy balance for a typical turbulence structure at the free surface. In the regime of weak turbulence, both parameters are small (typically $We_t \ll 1$, $Fr_t \ll 1$); there is little or no surface disturbances by the bulk eddies due to the stabilizing effect of the capillary and gravity forces. This effect is often referred to as a "blockage" effect. In the associated blockage layer, the velocity fluctuations are predominantly parallel to the interface. The existence of the blockage layer reduces the scalar transport in the vicinity of the interface. In this region, unlike the bulk region, heat or mass is mostly transferred by molecular diffusion (Kunugi et al., 2001). In strong turbulence ($We_t \gg 1$, $Fr_t \gg 1$), neither surface tension nor gravity can restrain the fluctuating eddies: the flow breaks up into drops, resulting in self-aeration (Volkart, 1980). A transitional region between weak and strong turbulence also exists that spans a substantial range of We_t and Fr_t. In such a region, free surface is substantially disturbed, but not broken. For brevity, in what follows we will refer to such flows and to the regime itself as transitional. In addition to the weak and strong turbulence regions, the diagram shows two other regions with

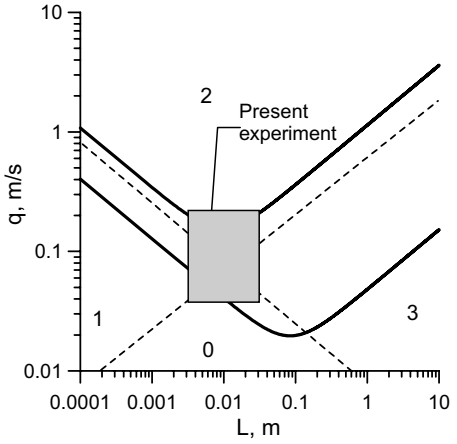

Fig. 1. L–q diagram adapted from Brocchini and Peregrine (2001) with the present experimental data. Region 0 is weak turbulence. Region 2 is strong turbulence. Region 1 is turbulence with surface tension dominant over gravity. Region 3 is gravity-dominated turbulence. The area between the two solid lines represents transitional region of marginal breaking.

no surface disintegration, in which gravity or surface tension is a major factor, and the surface phenomena associated with gravity or capillary waves are correspondingly dominant.

The main goal of the present study is to realize experimental conditions leading to the transitional flows and to study the peculiarities of the liquid–gas interface in this particular regime. An example of the flow in a transitional regime from the present experiment with inclined water flows is shown in Fig. 2. The turbulence structures from the flow bulk reach and deform the surface, resulting in an extremely non-flat interface. However, the surface deformations are not strong enough to produce droplets, as occurs in strong turbulence flows. These distinctive interface features can be seen in the flow side view (Fig. 2a) and from the data showing the time variations of the flow depth (Fig. 2b). An intermittence layer appears at the top of the flow, where the space is occupied by two different phases (air and water), and the bulk flow below is occupied with only one phase (water). The thickness of the intermittence layer in this particular flow near the side wall shown in Fig. 2a is about 30% of the mean flow thickness. However, in the side region, the results are strongly affected by the meniscus effect, resulting in higher values of both the intermittence layer and the flow depth. More representative information is given in Fig. 2b, where the experimental data for the fluctuating flow depth were taken at the middle of the experimental flume and are therefore free of the meniscus effect. From these data, the thickness of the intermittence layer, which can be roughly estimated as a distance between the lower and upper envelopes of the two-phase region, is only about 10% of the mean flow depth. A unique feature of the flow is a cell-type structure of the free surface, which can be seen in the images taken from above (Fig. 2c). The

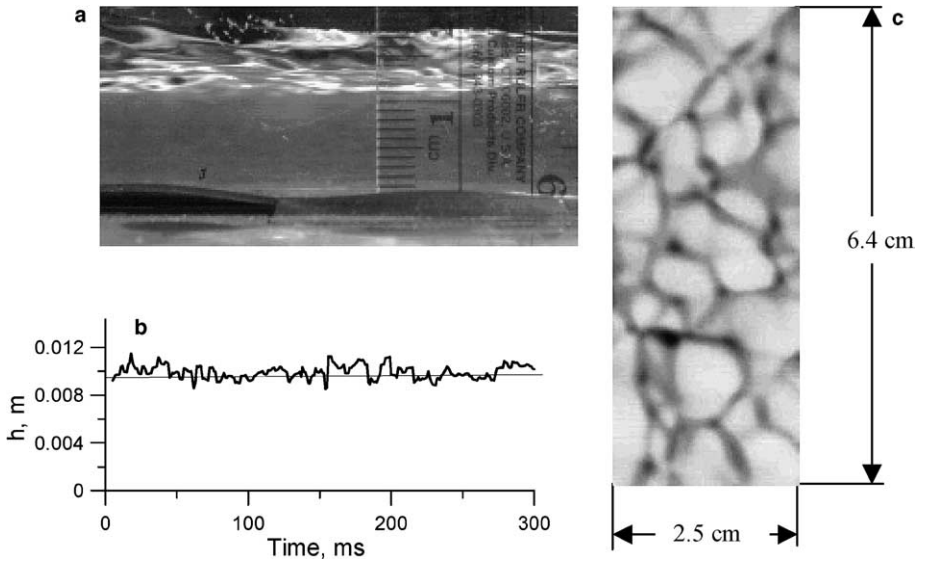

Fig. 2. Water–air interface in the regime from "weak" to "strong" turbulence: $\alpha = 3.5°$, $U_m = 1.43$ m/s, $h_m = 0.0093$ m ($Re = 13{,}250$, $Fr = 22.3$, $We = 261$). (a) The flow as viewed from the side through the transparent side wall. Two distinct layers can be seen. The upper layer is the intermittence region occupied by water and air, while the lower region is filled with water only. (b) Time variations of the flow depth measured with the ultrasound transducer at a point location, 3.5 m downstream of the nozzle at the middle of the flume. (c) A picture taken from above the free surface shows cell-type structures at the surface, which appear mostly as a result of turbulence–interface interactions.

experimental polygon, where the basic measurements were performed in the transitional regime, is also shown in the L–q diagram (Fig. 1). This polygon matches the transitional region, and suggests an about equal effect of gravity and surface tension. The lower and upper edges of the experimental polygon are, however, inside the weak and strong turbulence regions correspondingly. Therefore, the experimental data span the whole gap between weak and strong turbulence.

Realizing the transitional regime in fusion applications can be very favorable. The most attractive feature is that the surface blockage effect is reduced. Thus, better conditions for heat transfer via enhanced turbulent mixing at the interface by the surface-renewal eddies can be established. Some improvement of heat transfer is also possible through the surface waves. Long waves (with wavelengths much longer than the flow depth) can carry a significant fraction of the flow but almost do not affect the scalar transfer rate. However, short waves (with wavelengths comparable with the flow depth or shorter) are capable of bringing fresh liquid from the flow bulk to the near-surface region and back and hence create an additional mechanism for heat transfer improvement. The mechanism of vorticity generation by steep capillary waves was clearly shown by Longuet-Higgins (1992). Taking into account typical flow depth in fusion applications of about 0.01 m (see Abdou et al., 1999), one can expect that for liquids with physical properties close to water, the effect of waves on the heat transfer rate is mostly associated with capillary waves (the wavelength shorter than 0.0174 m). The second advantage of the transitional regime is that neither big nor small droplets are generated by the flow, so that the surrounding plasma will not be contaminated with liquid injections. The experimental conditions that provide such a regime are described in the next section.

2. Experiment

2.1. Experimental loop

To realize conditions in which the stabilizing effect due to capillary or gravity forces is reduced and therefore the desirable flow regime is established, either the surface tension coefficient or gravity component normal to the free surface, $g_\perp$, can be reduced. The first alternative, however, involves experiments with several liquids. It was found to be more effective to run the experiments using an inclined flume and only one liquid, water, as a working fluid. By changing the flume inclination angle, α, the component of the gravity vector perpendicular to the free surface, can be varied as $g_\perp = g\cos\alpha$. Correspondingly, the effective Froude number built through $g_\perp$, increases as α grows. For example, an increase in the Froude number by a factor of 5 can be achieved by changing the inclination angle from zero (horizontal orientation) to about 75°.

The test section is a 4 m long, 0.4 m wide, and 0.15 m deep rectangular flume made of transparent plastic material (Lexan), allowing for visual observations and filming the flow from different angles. The working fluid is injected continuously into the test section by two centrifugal pumps through an adjustable nozzle mounted at the top of the flume. The flow rate was measured by a turbine flow meter manufactured by Emco. The nozzle height is adjusted to provide an inlet flow thickness closer to the equilibrium flow depth. All measurements are taken at the center of the flume, 3.5 m downstream of the flow inlet, where the mean flow is hydrodynamically fully developed. The fully developed flow regime was confirmed by measurements of the flow depth at

several downstream locations, and by calculations based on a "k–epsilon" model of turbulence (Smolentsev et al., 2002b). The flow aspect ratio (flow width/flow depth) is higher than 40, so that the flow at the center of the flume is free from the side-wall effects. No shear was imposed at the interface (no gas flow) and the flows were considered to be shear free. Special care was taken to reduce initial disturbances at the nozzle outlet. To do this, a honeycomb matching exactly the nozzle cross-sectional dimensions was mounted inside the nozzle. As a result, liquid flow was introduced into the flume without significant interfacial waves and with reduced turbulence. More detailed description of the experimental facilities is given in Freeze (2002).

The dimensional and basic dimensionless parameters are shown in Table 1. Here, U_m and h_m are the bulk velocity and the mean flow depth at the reference location. The dimensionless parameters responsible for the turbulence–interface interactions are the Reynolds, Froude and Weber numbers, which are defined as $Re = U_m h_m/\nu$, $Fr = U_m^2/g_\perp h_m$, and $We = \rho h_m U_m^2/\sigma$. Unlike the conventional Reynolds number definition based on the hydraulic diameter, the Reynolds numbers presented in the table are based on the flow depth. The friction velocity was not measured in the experiment. An accurate estimation for U_* can be obtained from the standard correlation for a fully developed turbulent channel flow (e.g. Pope, 2000):

$$U_m/U_* \approx 5\log_{10} 2Re - 2.4. \quad (1)$$

A rough estimation for U_m/U_* for the Reynolds numbers shown in Table 1 is ~20. Applying Eq. (1) results in the following range for the turbulent Froude and Weber numbers in the experiment: $0.33 < We_t < 1.98$ and $0.15 < Fr_t < 0.52$. These values also fit with the transitional regime.

Table 1
Flow parameters in the experiments

Run #	α (°)	U_m (m/s)	h_m (m)	δ (m)	w (m)	σ_w (m)	Re	Fr	We	G	R/h_m
1	3.5	1.43	0.0093	0.00051	0.0062	0.00024	13,250	22.3	261	0.96	67.6
2	3.5	1.93	0.0127	0.00083	0.0052	0.00022	24,500	30.0	648	0.96	39.5
3	5.0	1.65	0.0085	0.00062	0.0055	0.00017	14,000	32.7	317	0.88	20.3
4	5.0	2.14	0.0117	0.00093	0.0050	0.00027	25,000	39.9	734	0.89	10.7
5	10.0	2.06	0.0067	0.00069	0.0043	0.00012	13,750	65.3	389	0.62	5.27
6	10.0	2.63	0.0096	0.00095	0.0039	0.00012	25,250	74.3	909	0.59	2.42
7	10.0	2.99	0.0111	0.00110	0.0038	0.00014	33,250	83.6	1360	0.56	1.57
8	15.0	2.33	0.0058	0.00064	0.0038	0.00008	13,500	98.5	431	0.44	3.22
9	15.0	2.95	0.0083	0.00091	0.0037	0.00012	24,500	110	989	0.44	1.61
10	15.0	3.31	0.0097	0.00116	0.0038	0.00013	32,250	119	1460	0.47	1.21
11	20.0	2.45	0.0050	0.00066	0.0033	0.00010	12,250	129	411	0.39	3.05
12	20.0	3.25	0.0076	0.00104	0.0034	0.00010	24,750	150	1100	0.41	1.36
13	20.0	3.64	0.0090	0.00120	0.0036	0.00015	32,750	160	1630	0.39	0.95
14	25.0	2.54	0.0045	0.00060	0.0032	0.00011	11,500	161	398	0.31	2.75
15	25.0	3.50	0.0072	0.00102	0.0034	0.00009	25,000	192	1210	0.33	1.10
16	25.0	3.93	0.0085	0.00131	0.0035	0.00012	33,500	203	1800	0.36	0.82
17	30.0	2.67	0.0043	0.00062	0.0029	0.00008	11,500	196	420	0.28	2.48
18	30.0	3.64	0.0066	0.00101	0.0035	0.00010	24,000	237	1200	0.28	1.03
19	30.0	4.13	0.0080	0.00136	0.0037	0.00014	33,000	250	1870	0.32	0.74

The experiments were conducted at seven inclination angles from 3.5° to 30°. For each angle, experimental runs were performed with two or three different flow rates, which were roughly 5, 10, and 15 L/s. In each run, the local flow depth was measured as a function of time with a 10 MHz 3 mm V129-RM Panametrics ultrasound transducer (Fig. 2b). Additionally, the flow dynamics was recorded using a Redlake MotionPro 10000 high-speed camera located 50 cm above the free surface. Adequate lighting was supplied through two 500 W halogen bulbs located 1 m above the free surface. The observation window was 12 cm by 2.5 cm. A 0.2 cm-thick white Teflon sheet was attached to the outside surface of the bottom plate. As a result, the images taken by the camera are not the free surface images but projections of the free surface on the screen. Although non-identical, the most important features seen in these images, such as the wave celerity and typical turbulent structure size, remain essentially the same. From this point of view, in what follows we will not distinguish between these, and will refer to the images taken with the camera as free surface images. The surface images (Fig. 2c) demonstrate cell-type structures with a typical size comparable with the mean flow depth (roughly, two times smaller). Each cell represents an interface area with surface rise or fall. The changes in the light intensity in the images are related to the variations of the local flow depth and the surface curvature. However the present technique does not allow for matching the light intensity in the images with the actual surface displacements. Calibration of the light intensity distribution in units of the surface-normal displacements was not possible because ultrasound measurements were not synchronized in time with the surface images. Thus, there is some lack of surface-normal resolution in the experiment. Long gravity waves as well as interface irregularities in the millimeter range were also beyond the measurement capabilities. Table 1 shows the average values of the surface displacement calculated as a standard deviation of the fluctuating flow depth, $\delta = \sigma_h$; the average size of the cell at the free surface, w (defined as the square root of the average cell area); and its standard deviation, σ_w. The last two columns in the table introduce a dimensionless parameter, G, which stands for the contribution of the gravity forces, and the radius of curvature of the surface bulge, R. These parameters will be explained below.

2.2. Image processing techniques

The raw sequences of the images were preprocessed for optical noise and non-uniform light intensity effects. The resulting images were analyzed using a method based on the morphological reconstruction technique (Boomgard and Balen, 1992), so that individual features of the interface can be distinguished more effectively. In this technique, we convert black and white original images into mosaics-type pictures by analyzing intensity variations in the original images and segmenting observed structures (cells) on the surface. Segmentation of the cells touching each other is done using a watershed transform method (Adams, 1993; Jones and Soille, 1996). Fig. 3 shows original and converted images of a 6.4×2.0 cm area of the free surface. The converted image allows for easier digital treatment by extracting information on the cell size, shape as well as its in-plane displacements and deformation with time. Some cells in Fig. 3 are marked to demonstrate the tracking capabilities of the technique. Reasonable accuracy of boundary detection was achieved through series of tests and optimizations of the image processing code. However, a certain limit of accuracy exists due to limitations such as image quality, light distribution and flow characteristics. Optimization of key parameters in image processing code was performed using

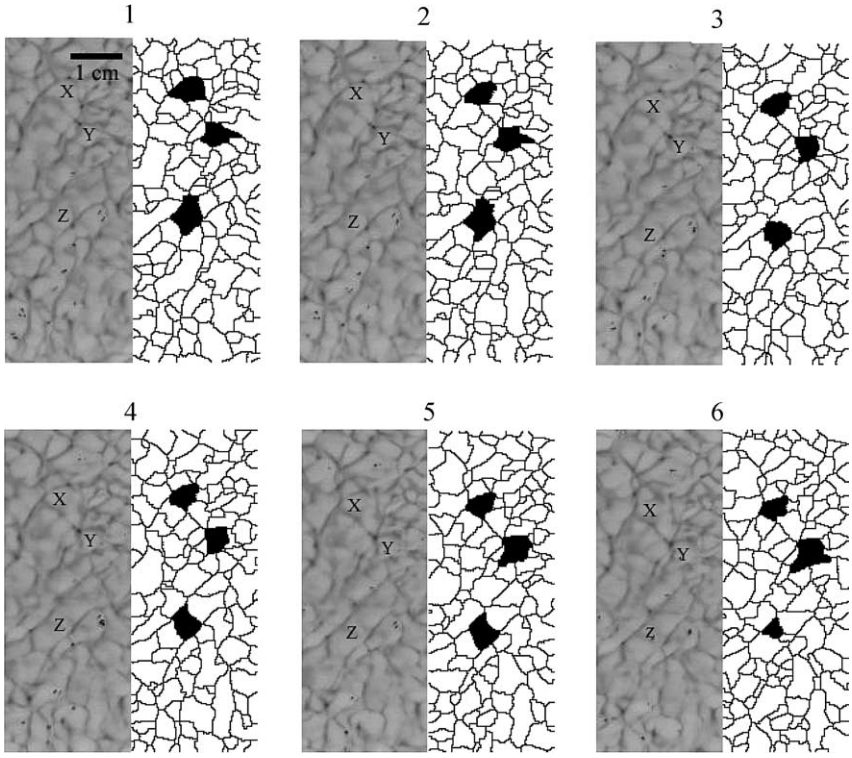

Fig. 3. Original (left) and converted (right) images of the free surface: $\alpha = 20°$, $U_m = 2.45$ m/s, $h_m = 0.0050$ m ($Re = 12{,}250$, $Fr = 129$, $We = 411$). The images are 1/2000 s apart.

visual comparisons between the processed images and original snapshots for several cases of Reynolds and Froude numbers. A minimum structure size, resolvable with the present image processing technique in the range of parameters listed in Table 1, is limited by the high-speed camera resolution and was estimated roughly to be 1 mm, with slightly higher resolution at lower flow velocities.

Fig. 4 demonstrates another image processing technique utilized in this work for cell tracking on the free surface in time. This technique is based on time recording of the intensity profiles of the original images within a narrow interrogation window. A narrow (2–3 pixels in width or about 50–60 μm) interrogation window was selected as demonstrated in Fig. 4a. At each moment of time the pixel intensity profile within the interrogation window is distinguished by high (black) and low (white) intensity pixels. High intensity pixels represent the cell boundary, while low intensity pixels correspond to the area inside the cell. Such intensity profiles taken at different moments of time, were then plotted together in the form of a two-dimensional graph shown in Fig. 4b. In this graph, the x coordinate shows the location along the interrogation window. The black and white streaks in the picture represent the phase trajectories of the cell boundary and its interior part correspondingly as the cell is convected downstream. The slope of the resulting patterns gives the velocity at which cells are convected downstream. The length of each streak shows an approximate lifetime of the traced cell inside the interrogation window.

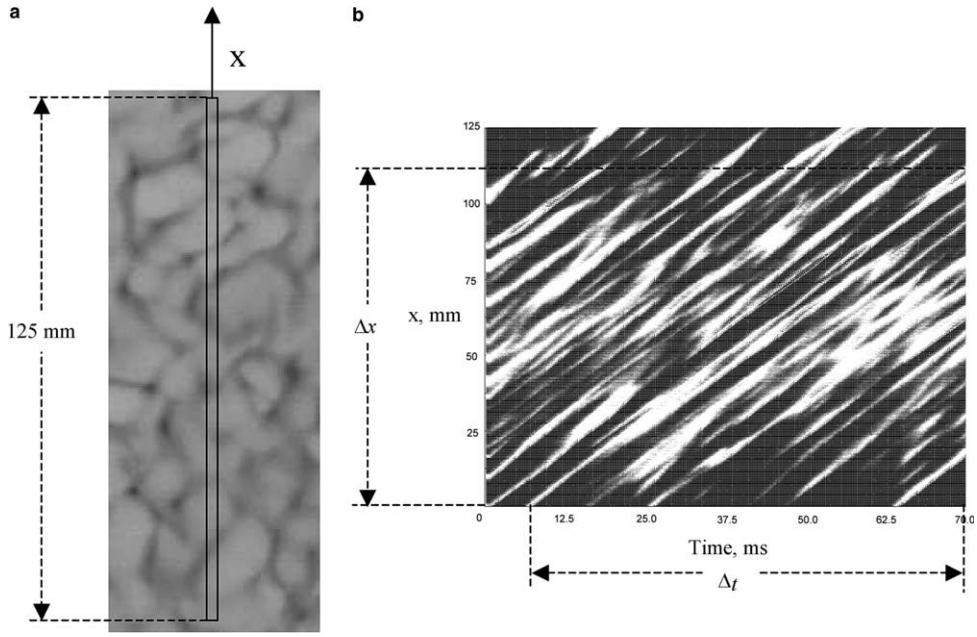

Fig. 4. Image processing technique for surface cell tracking and evaluation of the cell celerity: $\alpha = 5°$, $U_m = 1.65$ m/s, $h_m = 0.0085$ m ($Re = 14{,}000$, $Fr = 32.7$, $We = 317$). (a) Location of the interrogation window with flow direction from top to bottom. (b) Mapped intensity profiles in the x–t domain. Black and white streaks are related to the cell boundaries and the area within the cells respectively as the cells are convected downstream within the interrogation window. The cell celerity can be evaluated as $\Delta x/\Delta t = 0.11/64 \times 10^{-3} = 1.72$ m/s, which is very close to the bulk velocity shown in Table 1.

3. Experimental data and their analysis

The dimensionless parameters in the experiment were changed by varying the inclination angle and the flow rate. As the parameters *Fr* and *We* grow, the stabilizing effect due to gravity and capillary forces against the disrupting influence of turbulence decreases, and transition from weak to strong turbulence occurs. In the present experiment, transition to stronger turbulence is mostly caused by reduction in the gravity effect by changing the flume inclination angle and increasing the velocity. Correspondingly, the most significant variations, by more than ten times, occur in the Froude number. The other two parameters, *Re* and *We*, experience smaller changes. Hence, the changes in the experimental data are more attributed to the variations in the Froude rather than Weber number. That is why most of the experimental data presented in the paper were plotted as a function of *Fr*.

As the flow parameters change towards the strong turbulence regime, both frequency and amplitude characteristics of the flow depth experience significant changes. The power spectral density (PSD) distributions calculated with Welch's averaged periodogram method (Fig. 5) show a large peak at about 10–40 Hz, as well as a long "tail" of higher frequency modes. The large peak corresponds to the gravity, possibly roll waves, with a wavelength much longer than the flow depth. The higher frequencies are associated with the turbulence–interface interactions

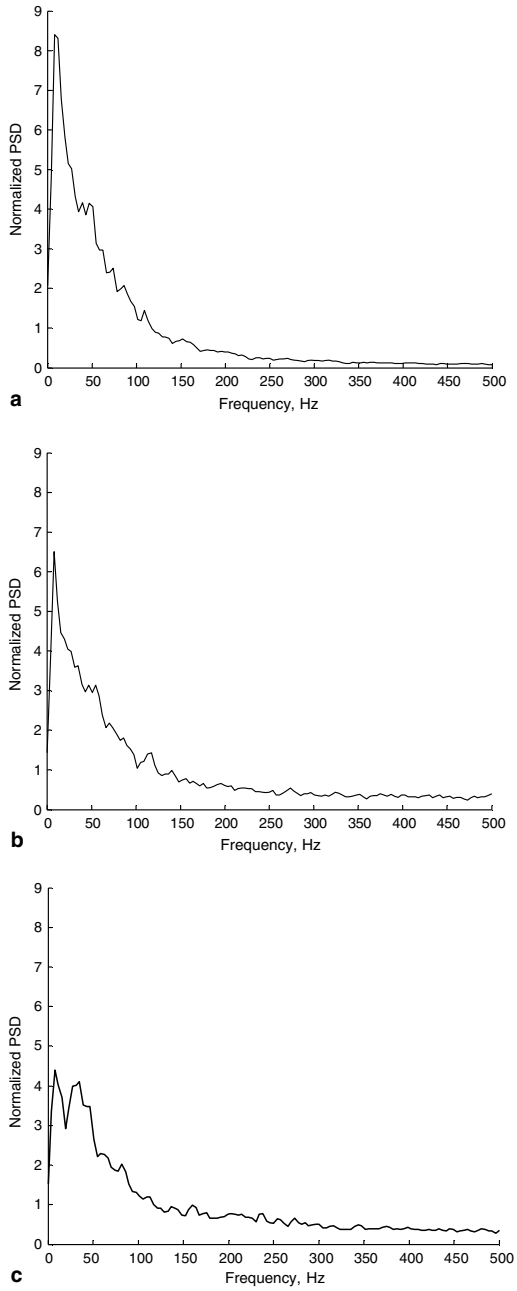

Fig. 5. Power spectral density (PSD) plots for the fluctuating flow depth: (a) $\alpha = 3.5°$, $U_m = 1.93$ m/s, $h_m = 0.0127$ m ($Re = 24{,}500$, $Fr = 30.0$, $We = 648$); (b) $\alpha = 15°$, $U_m = 2.95$ m/s, $h_m = 0.0083$ m ($Re = 24{,}500$, $Fr = 110$, $We = 989$); (c) $\alpha = 30°$, $U_m = 3.64$ m/s, $h_m = 0.0066$ m ($Re = 24,\ 000$, $Fr = 237$, $We = 1200$).

and shorter gravity and capillary waves. At higher *Fr*, the contribution of the higher frequencies becomes more significant, demonstrating more uniform spectra with a smaller maximum to

minimum ratio. The average amplitude of the pulsations of the flow depth also grows with *Fr* (Fig. 6). Both changes in the spectra and amplitude observed indicate more irregularities at the interface.

Although the long waves can carry a significant amount of liquid, the scalar transfer rate across the interface is mostly affected by the surface irregularities with a characteristic dimension comparable with the mean flow depth. Such structures can be seen in the surface images in the form of surface cells. Along with changes in the spectra and amplitude, one can observe changes in the surface cells. A clear tendency to form smaller structures at the surface as *Fr* grows can be seen in Fig. 7, where the mosaic surface images are shown at different inclination angles. This tendency is also summarized in Fig. 8, showing the average cell size as a function of *Fr*. The cell size in the figure is normalized with $[w] = (\sigma/\rho g_{\perp})^{1/2}$, which appears to be a better scale compared to $[w] = h_{\mathrm{m}}$ or to the scale based on the wall inner variables, $[w] = \nu/U_{*}$. The latter was introduced by Rashidi (1997) when describing the total surface patch area related to the bulk turbulence–free surface interactions in the weak turbulence flow. Introducing σ and $g_{\perp}$ under the present experimental conditions that match a transitional regime to strong turbulence seems to be reasonable, since both wave and turbulence structures at the free surfaces are affected by the surface tension and gravity effects. Plotting the data with this scale does not result in essential scattering of the experimental points as happens with two other scales. In addition, with this scale, the dimensionless data are around unity.

A special study was performed to address the surface cell celerity. The cell tracking technique described in Section 2 was applied to all experimental runs summarized in Table 1. It was found that in all cases the cell celerity is slightly (within a few percent) above the mean flow velocity. This fact shows clearly that cell origination is mostly related to the phenomenon of the turbulence–interface interactions but not caused by waves, whose celerity in both cases of gravity and capillary waves can be significantly different from the mean flow speed (Levich, 1962). However, there are traces of capillary waves, such as distortions of the streaks in the mapped intensity profiles in the *x*–*t* domain (Fig. 4), as well as distortions of the cells in the original or converted images as the

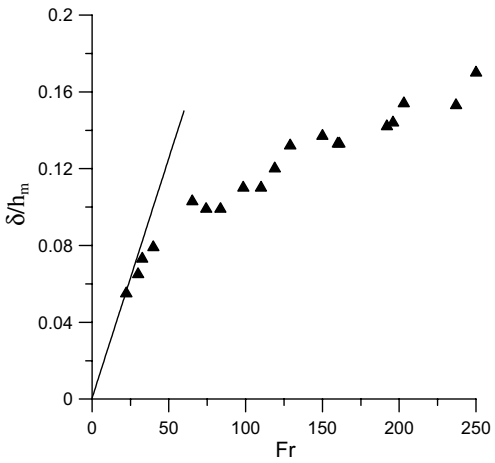

Fig. 6. Surface displacement normalized by the mean flow depth as a function of Froude number. The solid line, $\delta/h_{\mathrm{m}} = Fr/400$, is based on the Davies model (1972) for forces damping a turbulent eddy at a free surface.

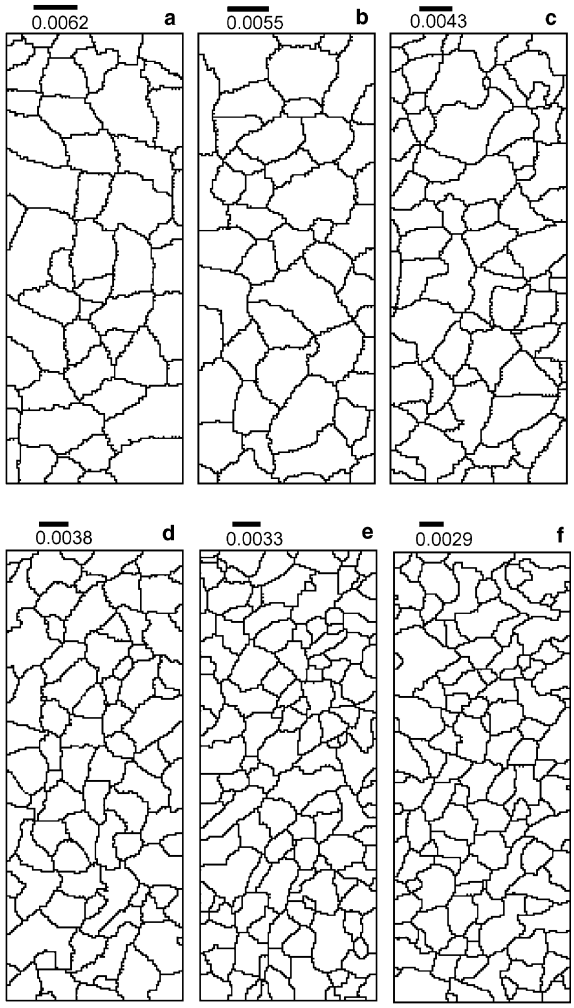

Fig. 7. Mosaic images of the free surface as approaching the strong turbulence regime from (a) to (f). Clear tendency to smaller cells can be seen as the Froude number grows (the average cell size is shown at the top of each frame). (a) $\alpha = 3.5°$, $U_m = 1.43$ m/s, $h_m = 0.0093$ m ($Re = 13{,}250$, $Fr = 22.3$, $We = 261$); (b) $\alpha = 5°$, $U_m = 1.65$ m/s, $h_m = 0.0085$ m ($Re = 14{,}000$, $Fr = 32.7$, $We = 317$); (c) $\alpha = 10°$, $U_m = 2.06$ m/s, $h_m = 0.0067$ m ($Re = 13{,}750$, $Fr = 65.3$, $We = 389$); (d) $\alpha = 15°$, $U_m = 2.33$ m/s, $h_m = 0.0058$ m ($Re = 13{,}500$, $Fr = 98.5$, $We = 431$); (e) $\alpha = 20°$, $U_m = 2.45$ m/s, $h_m = 0.0050$ m ($Re = 12{,}250$, $Fr = 129$, $We = 411$); (f) $\alpha = 30°$, $U_m = 2.67$ m/s, $h_m = 0.0043$ m ($Re = 11{,}500$, $Fr = 196$, $We = 420$).

cells are convected downstream (Fig. 3). Nevertheless, the capillary waves do not seem to be a driving mechanism here and their existence just introduces some insignificant variations in the surface images. The appearance of the cell structures in the surface images is thus mostly related to the upward motion associated with the turbulent eddies generated by the near-wall injections and their transformations once such eddies reach the interface. These motions result in the surface rises and falls, which in the plane surface images are manifested as the cell structures. The cells in the images move downstream with the mean flow velocity. The changes in their shape and size when moving downstream can be easily explained by the surface-normal displacements as well as

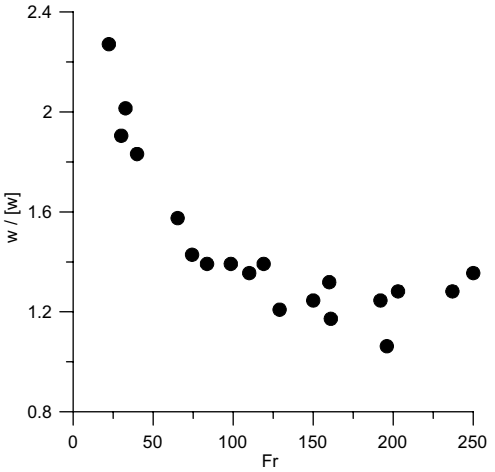

Fig. 8. Surface cell size scaled with $[w] = \sqrt{\sigma/\rho g_{\perp}}$ as a function of Fr.

their distortions due to eddy–eddy interactions and the capillary waves. It should be mentioned, that similar structures have been observed in the DNS studies for the weak turbulence flow (Handler et al., 1999). It is particularly remarkable that the cell size detected in the present experiment (roughly one half of the flow depth) is comparable with the size of the temperature patches calculated by Handler et al. (1999) (about one third of the flow depth). The present cell size also agrees with the experimental data by Komori et al. (1982, 1989) for the size of the turbulent eddy at the free surface (from one half to one flow depth) and with those by Rashidi (1997) for the surface patches (from about one half to one flow depth). This fact is another argument in support of the present idea that explains the cell appearance as a result of the bulk turbulence–free surface interactions.

The experimental data were also analyzed using a simple theory for the turbulent eddies near a liquid surface suggested by Davies (1972). According to Davies, when an eddy approaches from the bulk, it deforms the interface. At the point of equilibrium, a force balance exists in the following form:

$$\rho V_0^2 = \rho g_{\perp} \delta + 2\sigma/R. \tag{2}$$

In this equation the LHS is the pressure fluctuation associated with the motion of a turbulent eddy near the interface with the velocity V_0. The RHS is the sum of the gravitational pressure associated with the surface deflection δ, and the surface tension pressure related to the radius of curvature R of the deformation. Based on Davies, the eddy velocity at the free surface is very close to the friction velocity: $V_0 = U_*$. Such an assumption is not necessarily true in "deep flows" (i.e. natural river flows), where the turbulent eddies experience significant changes or even degrade before reaching the free surface. However, using this approximation seems to be reasonable here, in the laboratory conditions, as almost all the eddies reach the interface without losing their identity. Hence, Eq. (2) can be rewritten in a more convenient dimensionless form as follows:

$$1 = \frac{1}{2Fr_t^2}\frac{\delta}{h_m} + \frac{1}{We_t}\left(\frac{R}{h_m}\right)^{-1}. \tag{3}$$

Since the LHS of this equation is unity, the two terms on the RHS give the relative fractions in the net pressure balance. The first term, $G = (\delta/h_m)/(2Fr_t^2)$, associated with the gravity effect, can be directly calculated for all experimental runs using experimental values of δ and h_m and calculating U_* in Fr_t with Eq. (1). The second term is unknown but can be calculated from Eq. (3) by subtracting calculated values of G from 1. Eventually, the radius of the curvature of the turbulent eddy at the free surface can be calculated.

Both G and R/h_m are summarized in Table 1. One can see that for the first several runs in the table ($20 < Fr < 40$) the pressure balance is mostly contributed by the gravity force. Correspondingly, the surface deflection is controlled by the Froude number, such that $\delta/h_m = 2Fr_t^2$. A corresponding line is shown in Fig. 6 that demonstrates a very good match with the experiment. However at higher Fr, the second term on the RHS of Eq. (3) becomes more and more important and the simple proportionality of δ/h_m with the Froude number is not valid anymore. An attempt was made to estimate the second term by assuming a bell type shape for the surface deformation caused by an impinging eddy in the form of a normal error curve. Such a shape was observed in the experiments with water pulses approaching the water–air interface (Davies, 1972). For the shape given by the normal error curve, the radius of curvature is $R \sim l^2/8y_{max}$, where l is associated with the base of the surface bulge, and y_{max} is its maximum height. It will be reasonable here to consider $l = w$ and $y_{max} = \delta$. However, applying this approach to the present experimental data does not result in a good match. This fact may indicate that the shape of the surface deformations in the present experiment is different from the bell-type shape, or the theory by Davies itself is not quite accurate since the eddy motion in the near-surface region is more complicated than the model suggests. In this connection, it should be noted that Eq. (2) has not been derived rigorously from the flow equations and thus can not be considered as an exact solution, but more as an estimate. Correspondingly, the present calculations of the radius of curvature should be treated as approximate.

Although the experimental data do not directly allow for the turbulent eddy dimensions at the free surface, they can be used to interpret topological changes that occur with the turbulence structures near the free surface as the strong turbulence regime is approached. Three dimensions evaluated in the experiment can be associated, to some degree, with the eddy sizes near the free surface: the average surface deflection (δ/h_m), the surface cell size (w), and the average radius of curvature (R). As shown above (see Table 1 and Figs. 6 and 8), in the transition from weak to strong turbulence the surface deflection grows by about three times, while the other two dimensions decrease. The decrease in the cell size is about two times. The most significant changes occur within a relatively narrow range of Fr, from 20 to about 40–50. The changes in R/h_m are shown in Fig. 9. It is seen that at maximum Fr and We achieved in the experiment, R/h_m tends asymptotically to some value between 0.5 and 1, falling by more than an order of magnitude. These observations allow us to conclude that in the transition from weak to strong turbulence, the eddy topology near the free surface experiences significant change. In the regime of weak turbulence, the near-surface eddies are known to have a pancake-like structure and are predominantly two-dimensional. Similar flattened eddy structures appear in the present experimental runs when the Froude number is relatively small ($Fr < 50$). This is indirectly confirmed by relatively small values of the surface deflection ($\delta/h_m \sim 0.05$), large radius of curvature ($R/h_m \sim 10$), and relatively large surface cell size ($w/[w] \sim 2$). As the Froude and Weber numbers grow, both the gravitational and surface tension pressures become less resistant, allowing the turbulent eddy to move in the near-surface vicinity without being substantially deformed. For such eddies in the present

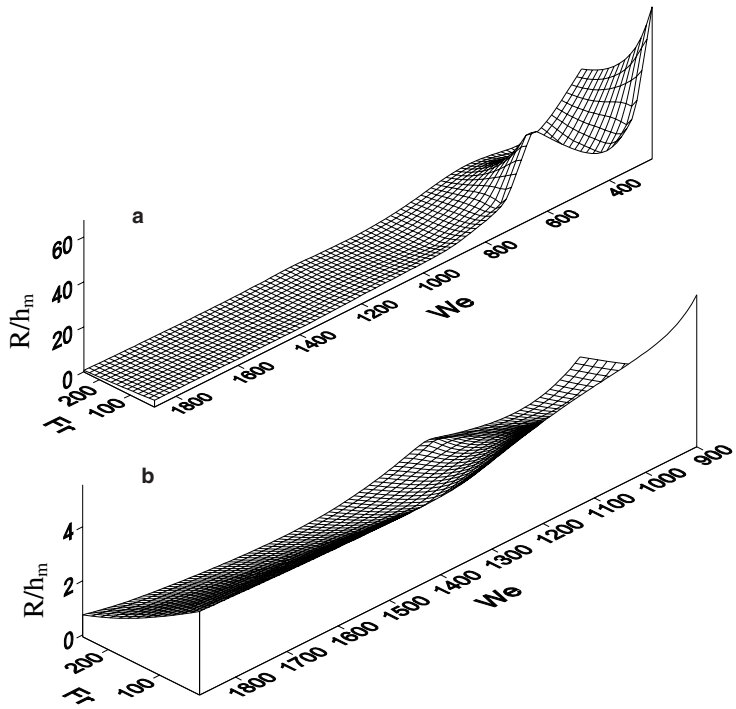

Fig. 9. Changes in the radius of curvature of the surface structure when approaching the strong turbulence regime from weak turbulence (increase in Fr and We): (a) full region; (b) part of the region at $We > 900$.

experiment: $\delta/h_m \sim 0.15$, $R/h_m \sim 0.5$–1, and $w/[w] \sim 1$. Therefore, the large surface deformations in the transitional regime are related to 3D rather than 2D structures, which resemble those in the bulk flow.

4. Conclusions

In the present experiments we have studied a turbulent water–air interface in inclined water flows in a long flume at high bulk Weber (<1900) and Froude (<250) numbers. The flow regime studied can be characterized as transitional from weak to strong turbulence, in which the free surface is significantly disturbed but not broken. The experiments were organized such that stronger turbulence was mostly achieved through the reduction of the gravity force, which in terms of the relevant dimensionless parameters corresponds to the increase of the Froude number based on the surface-normal component of the gravity vector. The experimental approach included measurements of the oscillating flow depth and imaging the flow surface by a high-speed camera. The raw experimental data were then used to get the most important statistical characteristics of the interface, such as the power spectral density, surface displacement, and size and celerity of the turbulent structures at the free surface.

The observations of the interface in the reference regime from weak to strong turbulence have resulted in an overall picture of the surface phenomena when the flow parameters are varied

towards stronger turbulence. Three types of disturbances are always present at the interface at the same time: long gravity waves, capillary waves, and turbulence cells appearing as a result of the turbulence–interface interactions. Among these three, in the range of the parameters studied, the turbulence–interface interaction seems to be the dominant one, and is mostly responsible for the typical cell-type structure of the interface observed in the experiment. The turbulence cells have a characteristic size (in the free surface plane) of about half of the mean flow depth. An important feature of the turbulence structures at the free surface, which suggests a principal difference with the surface waves, is their celerity. The celerity was evaluated using a newly developed interface tracking technique and is quite consistent with the mean flow velocity, while the celerity of both gravity and capillary waves has been known to be different from the mean velocity. Though small, the capillary waves can be detected in the power spectrum or through the variations of the shape of the turbulence structures at the interface as they move downstream. As the gravity effect is reduced (higher *Fr*), the contribution of the turbulence–interface interactions in the power spectrum becomes more pronounced; the amplitude of surface oscillations grows; and the average size of the turbulent patch at the surface decreases. This suggests that more turbulent structures (smaller in size) from the bulk flow reach and disturb the free surface, resulting in a highly agitated turbulent interface.

The reference regime from weak to strong turbulence can also be characterized in terms of the dimensions of a typical turbulent eddy at the free surface. In the weak turbulence regime, such structures are known to have a pancake shape observed in many experimental and DNS studies. The present studies also indicated significant flattening of eddies when approaching the free surface at $Fr < 40$–50. In this sub-regime, the gravity effect is dominant over the surface tension, and the experimental data for the surface displacement are in a good agreement with the theory for turbulent eddies near a free surface proposed by Davies. However, in most of the experimental runs performed at higher *Fr*, the contribution of gravity to the force balance is comparable to or even smaller than that due to the surface tension effect, so that a direct comparison of the theory with the present experimental data is not possible. The Davies theory was then used to estimate the radius of curvature of a typical surface deformation. As shown, the radius of curvature falls down asymptotically with *Fr* and *We* to a value from about half to one of the mean flow thickness. This fact suggests that in the transitional regime there is much similarity between the turbulent eddies at the free surface and those in the bulk flow and also shows that the large surface deformations are related to 3D rather than 2D structures.

The present study is a part of the ongoing work on turbulent open-channel flows. The results currently obtained have shown a need for further improvements of the experimental conditions and for a more rigorous theoretical basis for interpreting the experimental data. First, the shortcomings in the surface-normal resolution of the flow in the current approach should be overcome. This can be done by using the same experimental techniques but synchronizing in time the ultrasound measurements of the fluctuating flow depth with fast-speed camera acquisition. This would allow for fully 3D surface images by calibrating the camera pictures in units of the surface displacement. Second, there is a need for using more representative models for the turbulent eddy–free surface interaction. As a candidate, we can refer to a more modern model of the surface renewal theory based upon surface straining (SSM model) developed recently by Leighton et al. (2003). With this model, effects such as buoyancy, wave breaking, and surface shear can be included. However, modifying and then applying this model to the present experimental conditions

was beyond the purpose of the paper. Development of a more elaborate approach is planned to be a topic over next studies.

Acknowledgements

The authors would like to acknowledge the DOE support under grant DE-FG03-86ER52123 and express their gratitude to Prof. T. Kunugi from Kyoto University, Japan for his valuable comments and discussions. Contribution by Mr. B. Freeze in the beginning of the study is also gratefully acknowledged.

References

Abdou, M.A. et al., 1999. Exploring novel high power density concepts for attractive fusion systems. Fusion Eng. Des. 45, 145–167.

Adams, R., 1993. Radial decomposition of discs and spheres. Computer Vision, Graphics, and Image Processing: Graphical Models and Image Processing 55, 325–332.

Boomgard, R., Balen, R., 1992. Methods for fast morphological image transforms using bitmapped images. Computer Vision, Graphics, and Image Processing: Graphical Models and Image Processing 54, 252–254.

Borue, V., Orszag, S.A., Staroselsky, I., 2001. Interaction of surface waves with turbulence: direct numerical simulation of turbulent open channel flow. J. Fluid Mech. 286, 1–23.

Brocchini, M., Peregrine, D.H., 2001. The dynamics of strong turbulence at free surfaces. Part 1. Description. J. Fluid Mech. 449, 225–254.

Dankwerts, P.V., 1951. Significance of liquid-film coefficients in gas absorption. Ind. Eng. Chem. 43, 1460–1467.

Davies, J.T., 1972. Turbulence Phenomena. Academic Press, New York and London, p. 412.

Freeze, B., 2002. Wave structure and scalar transport at the free surface of turbulent flow on an inclined plane, Ph.D. Dissertation, UCLA.

Freeze, B., Smolentsev, S., Morley, N., Abdou, M., 2003. Characterization of the effect of Froude number on surface waves and heat transfer in inclined turbulent open channel water flows. Int. J. Heat Mass Transfer 46, 3765–3775.

Frisk, D.P., Davis, E.J., 1972. The enhancement of heat transfer by waves in stratified gas–liquid flow. Int. J. Heat Mass Transfer 15, 1537–1552.

Handler, R.A., Swean, T.F., Leighton, R.I., Swearingen, J.D., 1993. Length scale and the energy balance for turbulence near a free surface. AIAA J. 31, 1998–2007.

Handler, R.A., Saylor, J.R., Leighton, R.I., Rovelstad, A.L., 1999. Transport of a passive scalar at a shear-free boundary in fully developed turbulent open channel flow. Phys. Fluids 11, 2607–2625.

Jones, R., Soille, P., 1996. Periodic lines: definition, cascades, and application to granulometrie. Pattern Recognit. Lett. 17, 1057–1063.

Komori, S., 1996. Turbulence structure and CO_2 transfer at the air–sea interface and turbulent diffusion in thermally stratified flows, CGER Supercomputer Monograph Report, vol. 1.

Komori, S., Ueda, H., Ogino, F., Mizushima, T., 1982. Turbulence structure and transport mechanism at the free surface in an open channel flow. Int. J. Heat Mass Transfer 25, 513–521.

Komori, S., Murakami, Ya., Ueda, H., 1989. The relationship between surface-renewal and bursting motions in an open channel flow. J. Fluid Mech. 203, 103–123.

Kunugi, T., Satake, S., Sagara, A., 2001. Direct numerical simulation of turbulent free-surface high Prandtl number fluid flows in fusion reactors. Nucl. Instrum. and Meth. Phys. Res. A 464, 165–171.

Kutateladze, S., 1982. Semi-empirical theory of film condensation of pure vapors. Int. J. Heat Mass Transfer 25, 653–660.

Leighton, R.I., Smith, G.B., Handler, R.A., 2003. Direct numerical simulation of free convection beneath an air–water interface at low Rayleigh numbers. Phys. Fluids 15, 3181–3193.

Levich, V.G., 1962. Physicochemical Hydrodynamics. Prentice-Hall, p. 700.
Longuet-Higgins, M.S., 1992. Capillary rollers and bores. J. Fluid Mech. 240, 659–679.
Nagaosa, R., Handler, R.A., 2003. Statistical analysis of coherent vortices near a free surface in a fully developed turbulence. Phys. Fluids 15, 375–394.
Nakoryakov, V.E., Pokusaev, B.G., Radev, K.B., 1987. Waves and their effect on convective gas diffusion in falling liquid films. Zhurn. Prikl. Mekh. Tekh. Fiz. 3, 95–104 (in Russian).
Pope, S.B., 2000. Turbulent Flows. Cambridge University Press, p. 771.
Rashidi, M., 1997. Burst–interface interactions in free surface turbulent flows. Phys. Fluids 9, 3485–3501.
Saylor, J.R., Handler, R.A., 1997. Gas transport across an air/water interface populated with capillary waves. Phys. Fluids 9, 2529–2541.
Smolentsev, S., Abdou, M., Morley, N., Ying, A., Kunugi, T., 2002a. Application of the K-epsilon model to open channel flows in a magnetic field. Int. J. Eng. Sci. 40, 693–711.
Smolentsev, S., Freeze, B., Morley, N., Abdou, M., 2002b. Experimental study of turbulent supercritical open channel water flow as applied to the CLiFF concept. Fusion Eng. Des. 63–64, 397–403.
Smolentsev, S., Morley, N., Freeze, B., Miraghaie, R., Nave, J.-C., Banerjee, S., Ying, A., Abdou, M., 2004. Thermofluid modeling and experiments for free surface flows of low-conductivity fluid in fusion systems. Fusion Eng. Des. 72, 63–81.
Tsai, W.T., 1998. A numerical study of the evolution and structure of a turbulent shear layer under a free surface. J. Fluid Mech. 354, 239–276.
Ueda, U., Moller, R., Komori, S., Mizushina, T., 1977. Eddy diffusivity near the free surface of open channel flow. Int. J. Heat Mass Transfer 20, 1127–1136.
Volkart, P., 1980. The mechanism of air bubble entrainment in self-aerated flow. Int. J. Multiphase Flow 6, 411–423.